Quantitative evaluation of the impact of variation of optical parameters on the estimation of blood hematocrit and oxygen saturation for dual-wavelength photoacoustics

Subhadip Paul,[1] **Hari Shankar Patel,**[2] **and Ratan K. Saha**[1,*] (iD)

[1]*Department of Applied Sciences, Indian Institute of Information Technology Allahabad, Prayagraj, 211015, India*
[2]*Laser Biomedical Applications Division, Raja Ramanna Centre for Advanced Technology, Indore, 452013, India*
ratank.saha@iiita.ac.in

Photoacoustic (PA) spectroscopy is considered to be one of the most effective ways to measure the levels of hematocrit (H) and oxygenation saturation (SO_2) of blood, which are essential for diagnosing blood-related illnesses. This simulation study aims to investigate the impact of individual optical parameters, i.e., optical absorption coefficient (μ_a), scattering coefficient (μ_s), and anisotropy factor (g), on the accuracy of this technique in estimating the blood properties. We first performed the Monte Carlo simulations, using realistic optical parameters, to obtain the fluence maps for various samples. The wavelengths of the incident light were chosen to be 532, 700, 1000, and 1064 nm. Thereafter, the k-Wave simulations were executed, incorporating those fluence maps to generate the PA signals. The blood properties were obtained using the PA signals. We introduced variations in μ_a, μ_s, and g ranging from -10% to $+10\%$, -10% to $+10\%$, and -5% to $+1\%$, respectively, at 700 and 1000 nm wavelengths. One parameter, at both wavelengths, was changed at a time, keeping others fixed. Subsequently, we examined how accurately the blood parameters could be determined at physiological hematocrit levels. A 10% variation in μ_a induces a 10% change in H estimation but no change in SO_2 determination. Almost no change has been seen for μ_s variation. However, a 5% (-5% to 0%) variation in the g factor resulted in approximately 160% and 115% changes in the PA signal amplitudes at 700 and 1000 nm, respectively, leading to $\approx 125\%$ error in hematocrit estimation and $\approx 14\%$ deviation in SO_2 assessment when nominal $SO_2 = 70\%$. It is clear from this study that the scattering anisotropy factor is a very sensitive parameter and a small change in its value can result in large errors in the PA estimation of blood properties. In the future, *in vitro* experiments with pathological blood (inducing variation in the g parameter) will be performed, and accordingly, the accuracy of the PA technique in quantifying blood H and SO_2 will be evaluated. © 2024 Optica Publishing Group

1. INTRODUCTION

The generation of acoustic waves by any target tissue due to the absorption of light is known as the photoacoustic (PA) effect. Sir Alexander Graham Bell first observed the PA effect in 1880 [1]. The light-absorbing molecules, i.e., chromophores (like hemoglobin, myoglobin, melanin, etc.), are thermally excited by illuminating tissue with laser pulses of short duration and thus generating pressure waves, which can be captured in the form of PA signals (temperature rise in tissue is ≈ 0.1 K and pressure rise is ≈ 1 kPa) [2]. The PA microscopy (PAM) and tomography (PAT) techniques have been developed by exploiting the PA effect. These methods are able to display spatial distributions of hemoglobin concentration and oxygen saturation (SO_2) level of blood vessels of the imaging region (i.e., tissue) with an imaging depth of nm to mm range [3].

Therefore, both the anatomical information and functional information are retained in the PA imaging modality [4–6]. Yao *et al.* developed a special PAM called ultraviolet PAM (UV-PAM) for imaging of cell nuclei in intact biological tissue [7]. Sun *et al.* reported a method to use 3D multispectral quantitative PAT to measure hemoglobin concentration and tissue oxygenation at finger joints *in vivo* and evaluated its ability to detect osteoarthritis in the hand [8]. Recently, improved PA imaging devoid of different artifacts has been achieved with the help of machine learning, deep learning, and artificial intelligence methods [9–11].

The initial PA pressure rise (p_0) in a tissue due to absorption of light is given by $p_0 = \Gamma \mu_a F$, where Γ is the Grüeneisen parameter, F represents the fluence distribution in tissue, and

μ_a is the light absorption coefficient. It is clear that the PA pressure is linearly proportional to the light absorption coefficient of the tissue. Further, it is also linearly proportional to the fluence distribution, which is essentially governed by the scattering of the light beam inside the tissue. The scattering coefficient (μ_s) and anisotropy factor (g) dictate how photons will traverse inside the tissue through scattering events. In other words, these three optical parameters (μ_a, μ_s, and g) play a crucial role in the emission of PA waves from the tissue under investigation. A vast amount of research has been conducted to study and evaluate the optical parameters of blood. For example, Faber *et al.* conducted a study on the scattering properties of oxygenated and deoxygenated whole blood in the spectral range from 250 to 1100 nm. They performed a Kramers–Kronig analysis to determine the corresponding complex refractive indices [12]. Meinke *et al.* investigated the role of platelets and plasma (PLS) on the optical attributes of blood [13]. They also reported the optical behavior of simple blood samples, red blood cells (RBCs) suspended in phosphate buffered saline (PBS). Friebel *et al.* conducted a similar study with human blood in the spectral range from 250 to 2000 nm. The inverse Monte Carlo (MC) simulation was implemented to fetch those parameters from experimental data [14]. An excellent review of various works can be found in [15]. This study also illustrates how to calculate μ_a and μ_s of a blood sample at any arbitrary H level if those are experimentally obtained at any other H level.

PA investigations on blood samples have been performed by many groups in the context of PA imaging. Hochuli *et al.* extensively investigated the accuracy of the PA method for assessing the blood oxygen level and the role of selecting optimal wavelengths in their work [16]. Bench and Cox employed a multiwavelength linear unmixing technique to estimate intravascular SO_2 levels [17]. It is pertinent to note here that near-infrared (NIR) spectroscopy has also been widely used for monitoring tissue oxygen saturation as well as for functional imaging applications. More recently Sudakou *et al.* [18] have proposed a new method of data analysis based on a change in moments of distribution of time of flights of NIR photons that could potentially help in determining oxygen saturation of the different layers of tissue. The PA technique has also been employed to characterize blood samples *in vitro* [19–26]. The dual-wavelength PA technique works well for normal blood samples, where individual cells are suspended in a fluid medium (PBS or PLS). However, there are many pathological situations where RBCs deform, lose deformability, form aggregates, generate clumps, and explode, releasing hemoglobin molecules in the ambient medium [20,23,27]. For instance, RBCs become spherical and stiff in the case of malaria [28,29]; erythrocytes become greatly distorted in the case of Sickle cell disease, stomatocytosis, and echinocytosis [30,31]; RBCs build rouleaux for diabetic patients [32]; microclots indicate the early stage of thrombosis [19]; malaria and anemia can lead to hemolysis [24]. It may be anticipated that μ_s and g values for pathological blood samples will differ significantly with respect to the corresponding normal samples due to changes in shape, size, and spatial organization of cells. The fluence distribution is expected to be greatly affected by such a change, which in turn leads to a change in the PA signal. As a result of that, PA estimations of hemoglobin and oxygenation may become erroneous. We have conducted a simulation forward study to investigate the impact of variation of the optical parameters on the quantitative PA evaluations of the blood properties.

The objectives of the paper are as follows: i) to present the mathematical equations for calculations of optical parameters of blood samples utilizing published experimental data for subsequent PA signal simulations, ii) to obtain the blood hematocrit and oxygenation for various samples using spectroscopic relations, and iii) to quantify the effects of variations of the optical parameters on the PA estimation of the above-mentioned blood attributes. At first, we utilized the MC simulation technique to obtain the fluence maps of a series of blood samples. This study is conducted at four different wavelengths of the incident light (532, 700, 1000, and 1064 nm) [33–35]; then the k-Wave toolbox is integrated to produce the corresponding PA signals detected by a transducer with 7.5 MHz center frequency and 70% fractional bandwidth [36]. After that, the blood parameters are computed. Two types of blood samples were investigated: RBCs suspended in a PBS medium (referred to as the RBC + PBS in the remaining text); RBCs suspended in a PLS medium (denoted by RBC + PLS from now onwards). Finally, we have systematically introduced ±10% variations in μ_a, μ_s, and −5% to 1% variation in g values at 700 and 1000 nm for various test samples. For simplicity, one parameter (at both wavelengths) has been altered at a time keeping others fixed. The accuracy of the PA technique in assessing these blood parameters is quantified. It has been found that the anisotropy factor is the most critical parameter and a small change in the value of g can result in large errors in the H and SO_2 estimations for the dual-wavelength PAs.

2. MATERIALS AND METHODS

A. Definition and Calculations of Optical Parameters of Blood

1. Optical Absorption Coefficient

The optical absorption coefficient is defined as the amount of energy that is absorbed by a medium per unit length from an incident light beam of a single wavelength. The absorption of light energy takes place because of the presence of chromophores in the medium. It is given by

$$\mu_a = \sum_{j=1}^{J} C_j \epsilon_j, \tag{1}$$

where C_j and ϵ_j are the molar concentration and molar extinction coefficient for the jth species (chromophore). In blood, hemoglobin is greatly abundant and also the key absorber in the optical window (preferred for biomedical imaging). Other chromophores (e.g., lipids, collagen) have at least an order of magnitude lower absorption in this band [37]. Absorption of light energy causes Hb and HbO molecules to jump from one vibrational energy state to another. Measured PA signal arises predominantly from the Hb and HbO.

A healthy RBC typically encloses approximately 280 million hemoglobin molecules providing molar concentration (inside RBC), $C_{\text{Hb}} \approx 5.34 \times 10^{-3}$ moles/L. Consider that μ_{a,H_0}^{Hb} is the light absorption coefficient for a fully deoxygenated blood sample having hematocrit H_0. The absorption coefficient for such a solution is

$$\mu_{a,H_0}^{\mathrm{Hb}} = C_{\mathrm{Hb}} H_0 \epsilon_{\mathrm{Hb}} + H_0 f_{\mathrm{RBC}} \mu_a^W + (1 - H_0)\mu_a^M, \quad \textbf{(2)}$$

where f_{RBC} is the fractional water content in erythrocyte; μ_a^W and μ_a^M are the light absorption coefficients for water and the suspending medium (PBS or PLS), respectively. This sample is termed the reference sample. Hence, for a similar medium with hematocrit H, one can write

$$\mu_{a,H}^{\mathrm{Hb}} = C_{\mathrm{Hb}} H \epsilon_{\mathrm{Hb}} + H f_{\mathrm{RBC}} \mu_a^W + (1 - H)\mu_a^M. \quad \textbf{(3)}$$

If $\mu_{a,H_0}^{\mathrm{Hb}}$ is known beforehand then that of the latter sample can be estimated by utilizing the following formula:

$$\mu_{a,H}^{\mathrm{Hb}} = \frac{H}{H_0}\left[\mu_{a,H_0}^{\mathrm{Hb}} - H_0 f_{\mathrm{RBC}}\mu_a^W - (1 - H_0)\mu_a^M\right]$$
$$+ H f_{\mathrm{RBC}}\mu_a^W + (1 - H)\mu_a^M. \quad \textbf{(4)}$$

It is assumed here that the molar extinction coefficient remains the same for both samples. Analogously, for a fully oxygenated blood sample, one derives

$$\mu_{a,H}^{\mathrm{HbO}} = \frac{H}{H_0}\left[\mu_{a,H_0}^{\mathrm{HbO}} - H_0 f_{\mathrm{RBC}}\mu_a^W - (1 - H_0)\mu_a^M\right]$$
$$+ H f_{\mathrm{RBC}}\mu_a^W + (1 - H)\mu_a^M. \quad \textbf{(5)}$$

Therefore, the absorption coefficient of a blood sample with arbitrary H and $\mathrm{SO_2}$ levels can be readily calculated by utilizing Eqs. (4) and (5) as

$$\mu_{a,H} = \left[\eta \mu_{a,H}^{\mathrm{HbO}} + (1 - \eta)\mu_{a,H}^{\mathrm{Hb}}\right], \quad \textbf{(6)}$$

where $\eta = \mathrm{SO_2}$ is the oxygen saturation level of the blood sample. Experimentally measured μ_a spectra for fully deoxygenated and oxygenated hemoglobin solutions at $H_0 = 33.2\%$ can be found in Fig. 1 of [14]. Taking these data as the reference data, numerical values of μ_a for fully deoxygenated and oxygenated samples at any hematocrit level can be calculated employing Eqs. (4) and (5). For instance, plots of μ_a spectra for deoxygenated and oxygenated hemoglobin solutions at $H = 20\%$ are shown in Fig. 1A. The corresponding μ_a curves for solely PBS and PLS media are plotted in Fig. 1D (regenerated from Fig. 1 of [13]).

2. Optical Scattering Coefficient

The scattering coefficient describes how much energy of a monochromatic incident light beam will be dispersed by a scattering medium of unit length. It is a measurable quantity. It is proportional to the product of the hematocrit, hematocrit-dependent scaling factor $\beta(H)$, and scattering cross-section (σ_s):

$$\mu_{s,H_0} = H_0 \beta(H_0)\,\sigma_s. \quad \textbf{(7)}$$

The scattering cross-section for suspending particles of blood (i.e., RBCs) is a fundamental quantity and it depends upon the size and shape of RBCs, and the wavelength of the incident optical beam. Here we assume that the cells are identical in size and shape. In other words, it does not depend upon the level of dilution of the sample, allowing us to write [15]
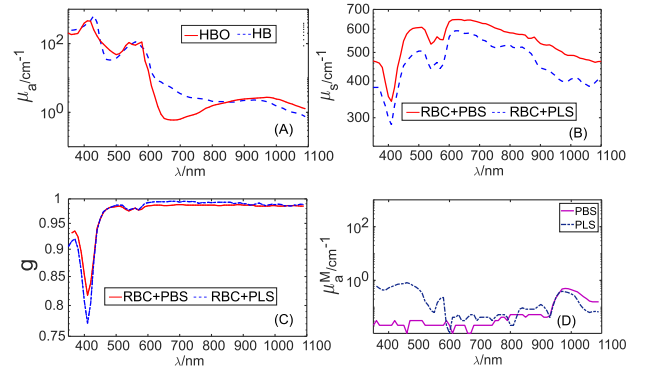
Fig. 1. (A) The spectra for the optical absorption coefficient for fully oxygenated and deoxygenated hemoglobin solutions at $H = 20\%$ (reference data for $H_0 = 33.2\%$ taken from Fig. 1 of Friebel *et al.* [14] and scaled them properly, using Eqs. (4) and (5), to generate data for $H = 20\%$). (B) The spectra for optical scattering coefficient for blood samples for two different suspending media at the same hematocrit level $H = 20\%$ (reference data for $H_0 = 8\%$ taken from Fig. 4 of [13]); Eq. (9) is used to generate these curves. (C) Plots of scattering anisotropy factor (data taken from Fig. 4 of [13]). (D) The optical absorption spectra for PBS and PLS media (reproduced from Fig. 1 of [13]).

$$\frac{\mu_{s,H}}{\beta(H)\,H} = \frac{\mu_{s,H_0}}{\beta(H_0)\,H_0}, \quad \textbf{(8)}$$

where $\mu_{s,H}$ is the optical scattering coefficient for a blood sample with hematocrit H; $\mu_{s,H}$ and μ_{s,H_0} are evaluated at the same wavelength. The hematocrit-dependent scaling factor connects dependent (for the dense system) and independent (for the spare system) scattering scenarios. Various functional forms of $\beta(H)$ are available in the literature [38–40]. Equation (7) for $\beta(H) = (1 - H)^2$ yields [15]

$$\mu_{s,H} = \frac{(1 - H)^2 H}{(1 - H_0)^2 H_0}\mu_{s,H_0}. \quad \textbf{(9)}$$

Equation (9) provides a way to estimate the scattering coefficient of a blood sample with a known hematocrit level using that of a reference sample. Note that the first sample with hematocrit H_0 is considered as the reference blood sample. Further, μ_{s,H_0} is known *a priori*.

Experimental estimations of μ_s spectra for RBC + PBS and RBC + PLS samples at $H_0 = 8\%$ are presented in Fig. 4 of [13]. Accordingly, one can easily obtain the μ_s spectrum at any hematocrit level utilizing Eq. (9). For example, μ_s spectra for RBC + PBS and RBC + PLS suspensions at $H = 20\%$ are displayed in Fig. 1B.

3. Scattering Anisotropy Factor

The anisotropy factor is a measure of the amount of forward direction retained with a scattering event. Consider a randomly polarized light beam scattered by an optical inhomogeneity. Let S_{11} be the scattered intensity along the angle θ concerning the forward direction. Its component along the forward direction is $S_{11}\cos\theta$. Accordingly, the g factor, which is the mean of $\cos\theta$, is given by

$$g = \frac{\int_0^\pi S_{11} \cos\theta \sin\theta \, d\theta}{\int_0^\pi S_{11} \sin\theta \, d\theta}. \tag{10}$$

Light scattering by a spherical scatterer can be described analytically employing the Mie theory. Thus, the angle-dependent scattered intensity and subsequently, the g factor can be calculated easily using this framework [41]. The corresponding spectrum of g for a spherical scatterer of radius $a = 2.75 \, \mu m$ mimicking an RBC can be found in [42] when the cell is suspended in a PBS/PLS medium. The variation of the g factor with optical wavelength for real RBCs obtained from experimental data is reported too. Figure 1C presents such plots (taken from Fig. 4 of [14]). In general, the Mie-theory-based graphs differ significantly compared to the experimentally estimated g values [42].

B. Propagation of Photons in Tissue

The optical parameters mentioned above dictate how photons traverse through a tissue; μ_a controls the amount of photon deposition, whereas μ_s and g regulate its spatial profile. The radiative transfer equation (RTE) can faithfully model photon propagation in tissue. The diffusion equation (DE) is a special case of the RTE (when $\mu_a \ll \mu_s$, i.e., medium almost reaches the scattering isotropy) and has been extensively used. It is a valid model for the propagation of photons in both the ballistic and diffusion regimes ($<100 \, \mu m$). The RTE is expressed as [43,44]

$$\frac{1}{c}\frac{\partial \tilde{R}(\vec{r}, \hat{\zeta}, t)}{\partial t} = -\left(\hat{\zeta}.\nabla + (\mu_s + \mu_a)\right) \tilde{R}(\vec{r}, \hat{\zeta}, t)$$

$$+ \mu_s \left(\int_{4\pi} \tilde{R}(\vec{r}, \hat{\zeta}, t) f(\hat{\zeta}.\hat{\zeta}') \, d\Omega'\right)$$

$$+ \Sigma(\vec{r}, \hat{\zeta}, t), \tag{11}$$

where $\tilde{R}(\vec{r}, \hat{\zeta}, t)$ is the radiance; $\hat{\zeta}$ and $\hat{\zeta}'$ are the directions of incidence and scattering of photons; c is the speed of light in vacuum. Further, $f(\hat{\zeta}'.\hat{\zeta})$ is the Henyey–Greenstein phase function. Equation (11) is also called the Boltzmann equation. The Henyey–Greenstein phase function is defined as [45]

$$f(\hat{\zeta}.\hat{\zeta}') = \frac{1}{4\pi} \frac{(1-g^2)}{\left(1 + g^2 - 2g\hat{\zeta}.\hat{\zeta}'\right)}$$

and $\quad \int_{4\pi} (\hat{\zeta}.\hat{\zeta}') f(\hat{\zeta}.\hat{\zeta}') d\Omega = 1 \quad$ where $\quad \hat{\zeta}.\hat{\zeta}' = \cos\theta,$ (12)

where Ω is the solid angle and $\Sigma(\vec{r}, \hat{\zeta}, t)$ is the source term [46]; the scattered photon beam makes an angle θ with the incident photon beam. The time-independent form of Eq. (11) is

$$\left[\hat{\zeta}.\nabla + (\mu_s + \mu_a)\right] R(\vec{r}, \hat{\zeta})$$

$$= \mu_s \left(\int_{4\pi} R(\vec{r}, \hat{\zeta}) f(\hat{\zeta}.\hat{\zeta}') \, d\Omega'\right) + \Sigma(\vec{r}, \hat{\zeta}). \tag{13}$$

Analytical solutions of Eq. (13) are possible only for some simplistic geometries like infinite slab, homogeneous medium possessing spherical/cylindrical symmetry, etc. Otherwise, being an integro-differential equation solving RTE is in general a very complex mathematical task. It may be possible to solve this equation numerically for complex problems. Methods like the finite element method, path integral method, integral transport method, and MC simulations can be employed.

C. Generation of Photoacoustic Waves in Tissue

The time-dependent PA equation under stress and thermal confinements is presented as

$$\left(\vec{\nabla}^2 - \frac{1}{v^2}\frac{\partial^2}{\partial t^2}\right) p(\vec{r}, t) = -\frac{\beta}{C_P}\frac{\partial \mathcal{H}(\vec{r}, t)}{\partial t}, \tag{14}$$

where β, C_P, and $\mathcal{H}(\vec{r}, t)$ are the isobaric volume expansion coefficient, isobaric specific heat, and heating function (i.e., the amount of heat deposited per unit time per unit volume), and $p(\vec{r}, t)$ is the pressure at a location $\vec{r}$ at time t. For a harmonically varying incident laser beam, it may be given by

$$\mathcal{H}(\vec{r}, t) = I_0(\vec{r})\mu_a e^{-i\omega t}, \quad \text{where } I_0(\vec{r}, t) = \int_{4\pi} \tilde{R}(\vec{r}, \hat{\zeta}, t) d\Omega. \tag{15}$$

It may be mentioned here that the heating is caused by light absorption. If the corresponding light fluence rate is denoted by $F(\vec{r}, t)$, the heating function, for a delta function laser pulse, happens to be $\mathcal{H}(\vec{r}, t) = \mu_a F(\vec{r})\delta(t)$.

For the sake of completeness, various approaches to solving Eq. (14) are briefly discussed herein. Note that Eq. (14) is an inhomogeneous partial differential equation; the term present on the right-hand side is called the source term. The Green's function method has been extensively utilized to obtain a solution to Eq. (14) [47]. It provides an integral solution to the problem. Therefore, it is possible to obtain a solution for a source with an arbitrary shape and size (for an acoustically homogeneous source). The PA signal from an illuminated region containing many independent sources (e.g., RBCs suspended in blood) has also been calculated deploying the discrete particle approach [48]. In this framework, the PA fields from individual cells approximating as spheres are calculated first in the frequency domain and then the linear superposition principle is employed to estimate the resultant PA field. Subsequently, the inverse Fourier transform is implemented to obtain the collective PA signal. Equation (14) can be solved numerically as well. For example, in the k-Wave toolbox, first order partial differential equations are solved using the k-space pseudo-spectral method.

D. Photoacoustic Estimation of Blood Hematocrit and Oxygen Saturation

The peak-to-peak pressure from a PA signal can be obtained as

$$P_{pp} = \max[p(\vec{r}, t)] - \min[p(\vec{r}, t)]. \tag{16}$$

The total hemoglobin and blood oxygen saturation can be estimated as [20]

$$\text{THb} = C_{\text{HbO}} + C_{\text{Hb}} = \frac{P_{\text{pp}}^{\lambda_1} \times \Delta\epsilon^{\lambda_2} - P_{\text{pp}}^{\lambda_2} \times \Delta\epsilon^{\lambda_1}}{\epsilon_{\text{Hb}}^{\lambda_1} \times \epsilon_{\text{HbO}}^{\lambda_2} - \epsilon_{\text{Hb}}^{\lambda_2} \times \epsilon_{\text{HbO}}^{\lambda_1}} \quad \textbf{(17)}$$

and

$$\text{SO}_2 = \frac{C_{\text{HbO}}}{C_{\text{HbO}} + C_{\text{Hb}}} = \frac{P_{\text{pp}}^{\lambda_2} \times \epsilon_{\text{Hb}}^{\lambda_1} - P_{\text{pp}}^{\lambda_1} \times \epsilon_{\text{Hb}}^{\lambda_2}}{P_{\text{pp}}^{\lambda_1} \times \Delta\epsilon^{\lambda_2} - P_{\text{pp}}^{\lambda_2} \times \Delta\epsilon^{\lambda_1}}, \quad \textbf{(18)}$$

respectively, with $\Delta\epsilon^{\lambda} = \epsilon_{\text{HbO}}^{\lambda} - \epsilon_{\text{Hb}}^{\lambda}$. The total hemoglobin and oxygen saturation for various blood samples have been assessed from simulated PA signals by implementing Eqs. (17) and (18), respectively.

E. Computational Aspects

1. Computation of Optical Parameters

The simulation requires numerical values of μ_a, μ_s, and g for blood samples considered in this study. The simulations were carried out for four different wavelengths of the incident light (532, 700, 1000, and 1064 nm) for five different blood samples having hematocrit levels, $H = 10\%$ to 50%. The choice of the wavelengths was dictated by the fact that 700 and 1000 nm wavelengths are situated on either side of the isosbestic point of blood absorption spectra (800 nm). The other two wavelengths, 1064 and 532 nm, correspond to the fundamental and second harmonic wavelengths of the Nd:YAG laser. The 532 nm wavelength also happens to be close to the Q band of Hb absorption.

RBCs were either suspended in PBS or PLS. The oxygen saturation levels were fixed to $\text{SO}_2 = 70\%$ and 90%, resembling venous and arterial blood.

Taking the samples of Fig. 1 of [14] as reference samples, numerical values of μ_a of our samples were calculated employing Eqs. (4)–(6). The top two rows of Fig. 2 demonstrate how μ_a varies with H at each probing optical wavelength for $\text{SO}_2 = 70\%$ and $\text{SO}_2 = 90\%$, respectively. As expected, μ_a grows linearly with H. The estimated numerical values are also included in Supplement 1, Table S1 (rows: 4, 7, 10, and 13, columns: 3 to 12 for $\text{SO}_2 = 70\%$; and rows: 19, 22, 25, and 28, columns: 3 to 12 for $\text{SO}_2 = 90\%$). Note that the PBS solution absorbs light greatly above 1000 nm, whereas the contribution of the PLS medium becomes significant below 600 nm and above 1000 nm (see Fig. 1D). The contribution of the ambient medium is included while calculating the optical absorption coefficient of blood.

Similarly, plots of calculated values of μ_s for samples investigated in this study are presented in the third row of Fig. 2. These values were calculated using Eq. (9). The data sets for PBS and PLS media experimentally determined at $H = 8\%$ in Fig. 4 of [13] were considered as reference data. Figure 2 (third row) exhibits nonlinear variation with H for all optical wavelengths. The computed numerical values of μ_s are also included in Supplement 1, Table S1 (rows: 5, 8, 11, and 14, columns: 3 to 12, for $\text{SO}_2 = 70\%$; and rows: 20, 23, 26, and 29, columns: 3 to 12 for $\text{SO}_2 = 90\%$).
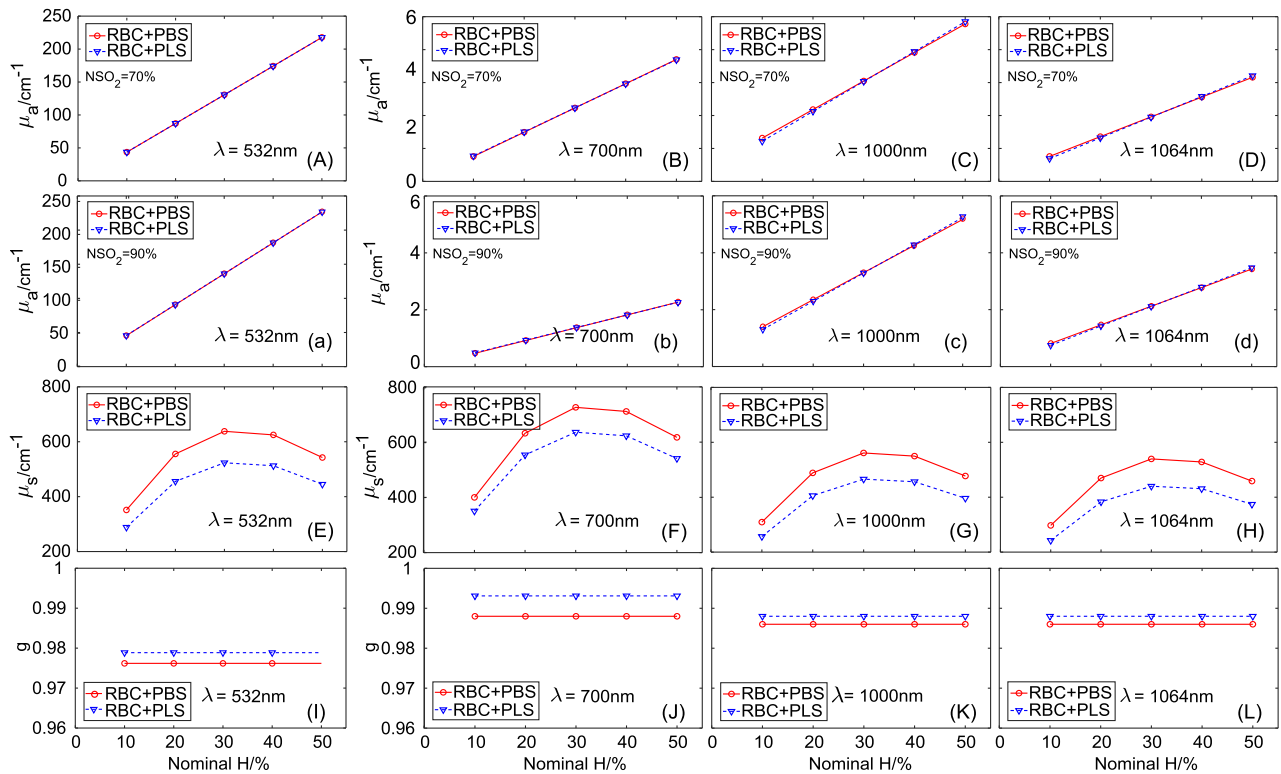
Fig. 2. The variations of μ_a, μ_s, and g at five different hematocrit levels (10% to 50%) at four different wavelengths of the incident light (532, 700, 1000, and 1064 nm). (a)–(d), (A)–(D) Plots of μ_a with H. (A)–(D) Nominal SO_2, $\text{NSO}_2 = 70\%$, and $\text{NSO}_2 = 90\%$ for (a)–(d). The third and fourth rows plot variations of μ_s and g with hematocrit at those optical wavelengths. The acronyms RBC + PBS and RBC + PLS indicate that RBCs are suspended in PBS and PLS media, respectively.

The plots of the g factor for our blood samples are incorporated in the fourth row of Fig. 2. The numerical values were taken from Fig. 4 of [14] as mentioned earlier. It is evident from Fig. 2 (fourth row) that the g values remain unchanged as they do not depend on H for both the surrounding media. The same values are also provided in Supplement 1, Table S1 (rows: 6, 9, 12, and 15, columns: 3 to 12, for $SO_2 = 70\%$; and rows: 21, 24, 27, and 30, columns: 3 to 12 for $SO_2 = 90\%$).

2. Simulation of Fluence Distributions

The MC multilayer (MCML) program [33] was employed for simulating the propagation of photons in homogeneous blood samples. The photon-beam made a 0° with the normal to the exposed surface. Photons were launched with a predefined weight w_0. The length l_s traversed by a photon between two successive scattering events was random. These path lengths (l_s) were determined following the function $-\frac{ln(\kappa)}{\mu_s}$, where κ was a uniformly distributed random number lying between zero and one. Near the boundary, the photon either shifts to a new location (if there is no boundary hit) or keeps a step forward depending on the nearest boundary distance (if there is a boundary hit), following which, depending on the Fresnel coefficient, the photon is either reflected back in the same medium or transmitted to the adjoining medium. The direction cosines of the reflected/transmitted photon are modified before moving it to the new position (by a distance equivalent to the remaining partial step size). The Henyey–Grenstein function was used to calculate the scattering angle, given as $P(\cos\theta) = \frac{1-g^2}{2(1-g+2g\cos\theta)^{3/2}}$. The azimuthal angle was selected from a uniformly distributed random number varying from zero to 2π. After each scattering event, the weight of the photon was reduced by a factor of $(1 - \delta w_0)$ with $\delta w_0 = \frac{\mu_a}{\mu_a+\mu_s}$. These steps (absorption and scattering) were repeated until the weight of the photon became less than a preset threshold value (in our case 10^{-4}). Finally, the Roulette method was used to check the survival possibilities of the photons. The idea was that when w_0 of a photon became lower than the threshold (w_{Th}), the photon had a single chance to survive and contribute to fluence distribution in an unbiased manner. To achieve this, the weight of the surviving photon was increased by a factor that is reciprocal to the probability of the survival in the Roulette test.

In this study, the tissue volume was discretized into $(n_x, n_y, n_z) = (150, 150, 150)$ voxels, with edges $dx = dy = dz = 0.005$ cm. The laser beam diameter was fixed to 0.05 cm. The optical properties of these voxels were chosen from Supplement 1, Table S1 depending upon the blood sample. The simulations were performed in a desk-top computer with specifications: Intel Core Intel Core i7 12700 CPU at 2.1 GHz, 12 cores, 12 logical processors, Microsoft Windows 11 Professional OS, 128.0 GB DDR5 RAM, 16 GB NVIDIA RTX A4000 GPU with GCC-6.3.0-1, and MATLAB 2023b. We employed 1 million photons in an MC simulation (average computation time was about 5 min). It may be mentioned here that other variants of MC simulation that include parallel architecture using a message passing interface (MPI) and graphics processing unit (GPU) programming for faster simulation of light propagation in layered tissues are also available in the literature [34,49].

Moreover, analytical solutions of the diffusion equation are also available for a medium with multiple planner interfaces, which permits accurate estimation of fluence distribution in multi-layered tissue [18,35].

3. Simulation of PA Signals

The MC simulation provided the 3D fluence matrix for each sample. After that, the k-Wave simulation was performed to simulate the dynamics of the propagation of PA waves in 3D. A schematic of the simulation setup is shown in Fig. 3. The initial pressure rise for individual voxels was computed to be $p_0 = \Gamma\mu_a F$. The size of the simulation domain was taken to be $(N_x, N_y, N_z) = (170, 170, 220)$ grid points with $dx = dy = dz = 0.005$ cm. The speed of sound and density of the sample and coupling medium were set as $v_{Blood} = v_{Med} = 1500$ m/s and $\rho_{Blood} = \rho_{Med} = 1000$ kg/m^3, respectively. The width of the perfectly matched layer (PML) was assigned to be 0.05 cm. The PML prevents unwanted boundary reflections of acoustic waves. An anisotropic absorption coefficient of 100 np/m was set inside the PML. The time-dependent PA pressure data were stored for grid points situated within the circular region resembling a flat transducer with a radius of 0.05 cm and consisting of $N_{sp} = 317$ grid points. Its center was located at $(N_x/2, N_y/2, N_z - 15)$. The center frequency and fractional bandwidth of the sensor points were specified to be 7.5 MHz and 70%, respectively. The PA signal for each sample was computed by summing up sensor data and subsequently, the peak-to-peak amplitude was evaluated for estimating the H and SO_2 levels from Eqs. (17) and (18). The simulations were executed in the same computer enabling the GPU environment. The computation time was about 14 s per simulation.

4. Impact of Variation of Optical Parameters on the Assessment of Blood H and SO_2

In the next stage, we systematically studied the impact of variation of the optical parameters on the PA estimation of blood H and SO_2 using PA signals simulated at 700 and 1000 nm and implementing Eqs. (17) and (18). Here we considered a series of blood samples at fixed $H = 40\%$ but with $SO_2 = 70\%$ and $SO_2 = 90\%$. For the first class of samples, the numerical values of μ_a at 700 and 1000 nm were jointly varied from -10% to 10%; however, μ_s and g were kept constant (see rows 3 to 12 of Supplement 1, Table S2) ($\mu_s = 711.15$ cm^{-1}, $g = 0.988$ at
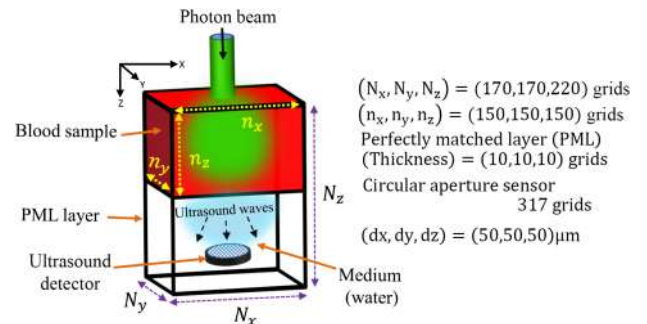
Fig. 3. Computational models for the Monte Carlo and k-Wave simulations [33,36].

700 nm; $\mu_s = 549.74$ cm^{-1}, $g = 0.986$ at 1000 nm). For the second set of samples, μ_s was altered from -10% to 10% at each wavelength; nevertheless, we did not vary μ_a and g (see rows 13 to 22 of Supplement 1, Table S2). For the third group of samples, g values were unitedly changed from -5% to 1% at these wavelengths but μ_a and μ_s were kept fixed (see rows 23 to 36 of Supplement 1, Table S2). The samples, with 0% variation, served as the controls for those groups. The role of the g factor was further assessed at various hematocrit levels; for the first, second, and third groups hematocrits were fixed at $H = 20\%$, 30%, and 40%, respectively. Supplement 1, Table S3 includes the numerical values of the optical parameters of these classes of samples.

3. NUMERICAL RESULTS

Figure 4 displays the spatial distributions of sensitivity to absorption for the blood samples having hematocrit levels $H = 10\%$ and 50%. The maps are shown for four different wavelengths of the incident light (532, 700, 1000, and 1064 nm) and also for two surrounding media with $SO_2 = 70\%$ [Figs. 4A–H for PBS and 4(a)–(h) for PLS]. Similarly, Figs. 4I–4P and 4(i)–4(p) demonstrate the same maps but for $SO_2 = 90\%$. The photons penetrate more at higher wavelengths (700, 1000, 1064 nm) and least at 532 nm (compare rows from 1 to 4). For $H = 50\%$, the magnitudes of absorbance maps are stronger in the top layers compared to those of $H = 10\%$ (compare columns 1, 3; 2, 4; 5, 7; and 6, 8). The contours corresponding to the RBC + PLS samples are more stretched in the forward direction rather than the lateral direction, whereas this pattern is less prominent for the RBC + PBS samples (compare columns 1, 2; 3, 4; 5, 6; and 7, 8).

The PA signals for a series of samples were computed using the respective fluence distributions. Some representative signals are shown in Supplement 1, Fig. S1. Accordingly, the hematocrit and oxygen saturation levels were estimated for each sample. The plots of the estimated hematocrit levels for various samples are shown in Figs. 5A–5F for different wavelength pairs of the incident light. To convert the PA estimate of H into the absolute H of a sample, the sample with the highest hematocrit, $H = 50\%$, has acted as the calibrating system. The estimated and nominal H values in general exhibit a close match. The estimation error is maximum at $H = 30\%$ (see top row of Fig. 5). However, in Fig. 5F, estimation error increases as the hematocrit decreases.

The plots in Figs. 6A–6F represent variations of the evaluated SO_2 at different hematocrit levels. The assessed SO_2 levels are almost close to the nominal value, $SO_2 = 70\%$ at 532–700 nm (maximum estimation error $\approx 14\%$, Fig. 6A), 700–1000 nm (highest estimation error $\approx 10\%$, Fig. 6D), and 700–1064 nm (maximum estimation error $< 8\%$, Fig. 6E) wavelength pairs. The errors are comparable for $SO_2 = 90\%$ as well. In the rest of the figures, i.e., for 532–1000, 532–1064, and 1000–1064 nm wavelength combinations, the estimated SO_2 values demonstrate drastic variations and become mostly unrealistic.

The next step has been to systematically vary μ_a, μ_s, g and accordingly, study how they impact PA estimations of the hematocrit and oxygen saturation levels. The hematocrit and oxygen saturation levels have been fixed at $H = 40\%$ and $SO_2 = 70\%$ and $SO_2 = 90\%$, respectively for this investigation. Further, saline water has been chosen as the surrounding medium. The simulation results are detailed in Fig. 7. Figures 7A and 7(a) confirm that peak-to-peak amplitude grows linearly with increasing μ_a. A 10% change in μ_a causes approximately the same amount of change in the peak-to-peak amplitude at 700 nm (also in 1000 nm). This is expected as the PA amplitude is linearly proportional to μ_a. The same trend is
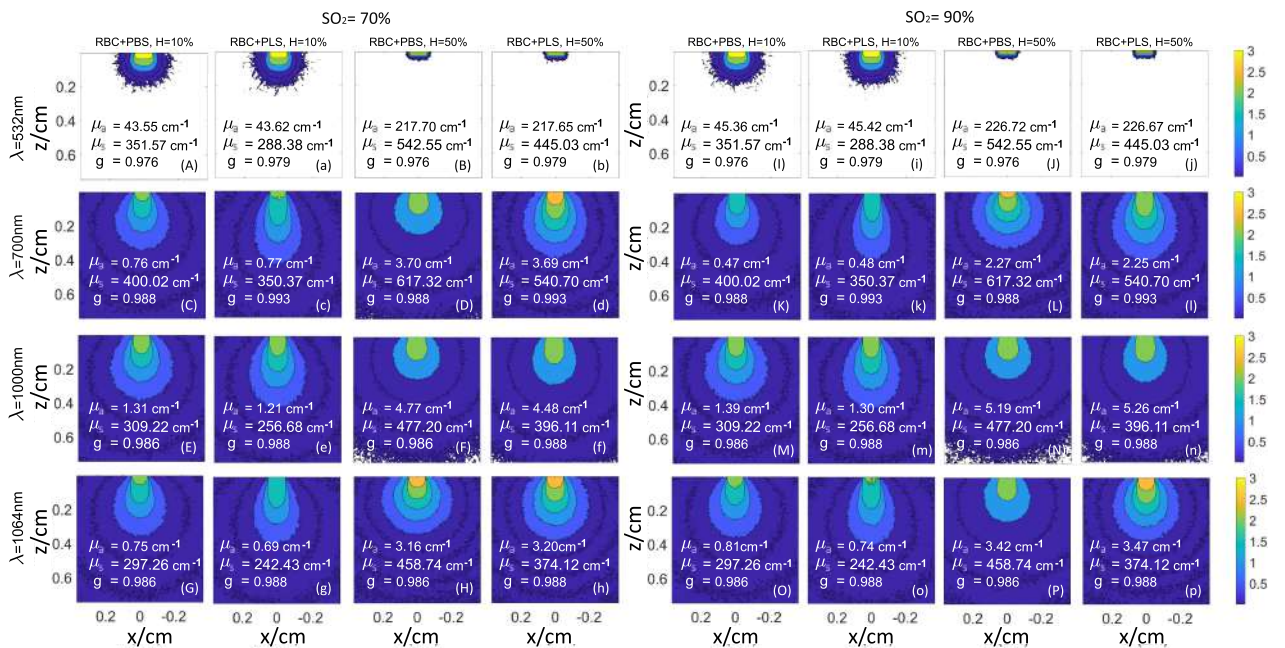
Fig. 4. Contour plots of spatial distribution of sensitivity to absorption (in log scale) for various wavelengths of the incident light (532, 700, 1000, and 1064 nm) in blood samples with $H = 10\%$ and 50%. (A)–(H) RBCs are suspended in PBS; (a)–(h) RBCs are surrounded by the PLS medium. In all plots, SO_2 is fixed to 70%. (I)–(P), (i)–(p) Same plots but for $SO_2 = 90\%$.
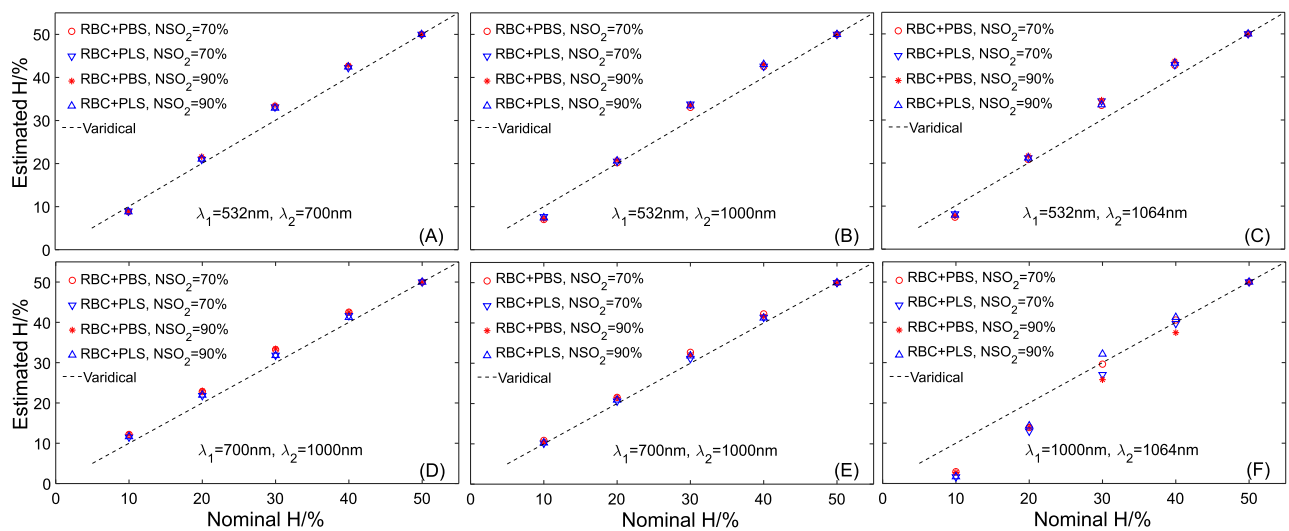
Fig. 5. The plots of the estimated versus nominal H for six different wavelength pairs. Results are shown for two different suspending media (PBS and PLS) (nominal SO_2, $NSO_2 = 70\%$ and 90%).
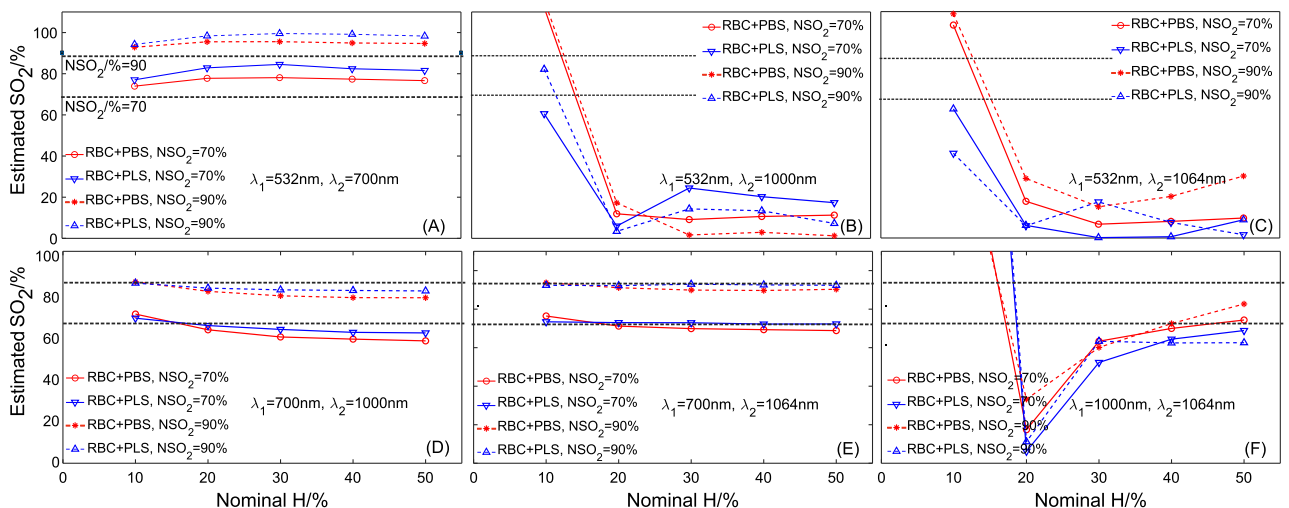

Fig. 6. The graphs present how estimated SO_2 varies with hematocrit at six different wavelength pairs for two cases, RBCs surrounded by PBS and PLS, respectively (nominal SO_2, $NSO_2 = 70\%$ and 90%).

also observed in the estimation of blood hematocrit (Fig. 7D). Nevertheless, such a variation does not impact the assessment of blood SO_2 (Fig. 7G). The peak-to-peak amplitude almost remains constant though μ_s is altered from -10% to 10% at each optical wavelength as can be seen from Figs. 7B and 7(b) (compare the peak-to-peak values at 0% and 10% variations). Moreover, both evaluations agree well with the nominal values (Figs. 7E and 7H, respectively). Significant variation of peak-to-peak amplitude occurs when g is altered [see Figs. 7C and 7(c)]. This quantity decreases as g increases; a more than two-fold rise of peak-to-peak amplitude is computed for a 5% reduction of g (compare the peak-to-peak values of PA signals at 0% and -5% variations at 700 nm as well as in 1000 nm). The PA method overestimates/underestimates the blood hematocrit level if g is less/more than the actual value (see Fig. 7F). The trend is the opposite if the PA technique is applied for the determination of blood SO_2 (see Fig. 7I).

It is interesting to note from Fig. 7 that a small variation of the g factor can result in a large error in the PA estimations of the blood H or SO_2. Therefore, it is a natural question, how the g factor would affect PA estimates at various hematocrit (H) levels. This section addresses this issue. Figure 8 illustrates the simulation outcomes at $H = 20\%$, 30%, and 40%. For convenience and completeness, the same graphs of Figs. 7C, 7(c), 7F, and 7I are pasted here too. The peak-to-peak amplitude as seen previously monotonically decreases with increasing g for all hematocrit levels (see top two rows of Fig. 8). The hematocrit estimation manifests the same errors in all cases (e.g., compare -5% and 0% variations in the third row in Figs. 8D–8F). Similarly, the errors in SO_2 estimation are almost identical (fourth row of Figs. 8G–8I). Therefore, the errors for assessing the H and SO_2 values induced by the fluctuation of g are comparable. However, for SO_2 estimation, the error increases
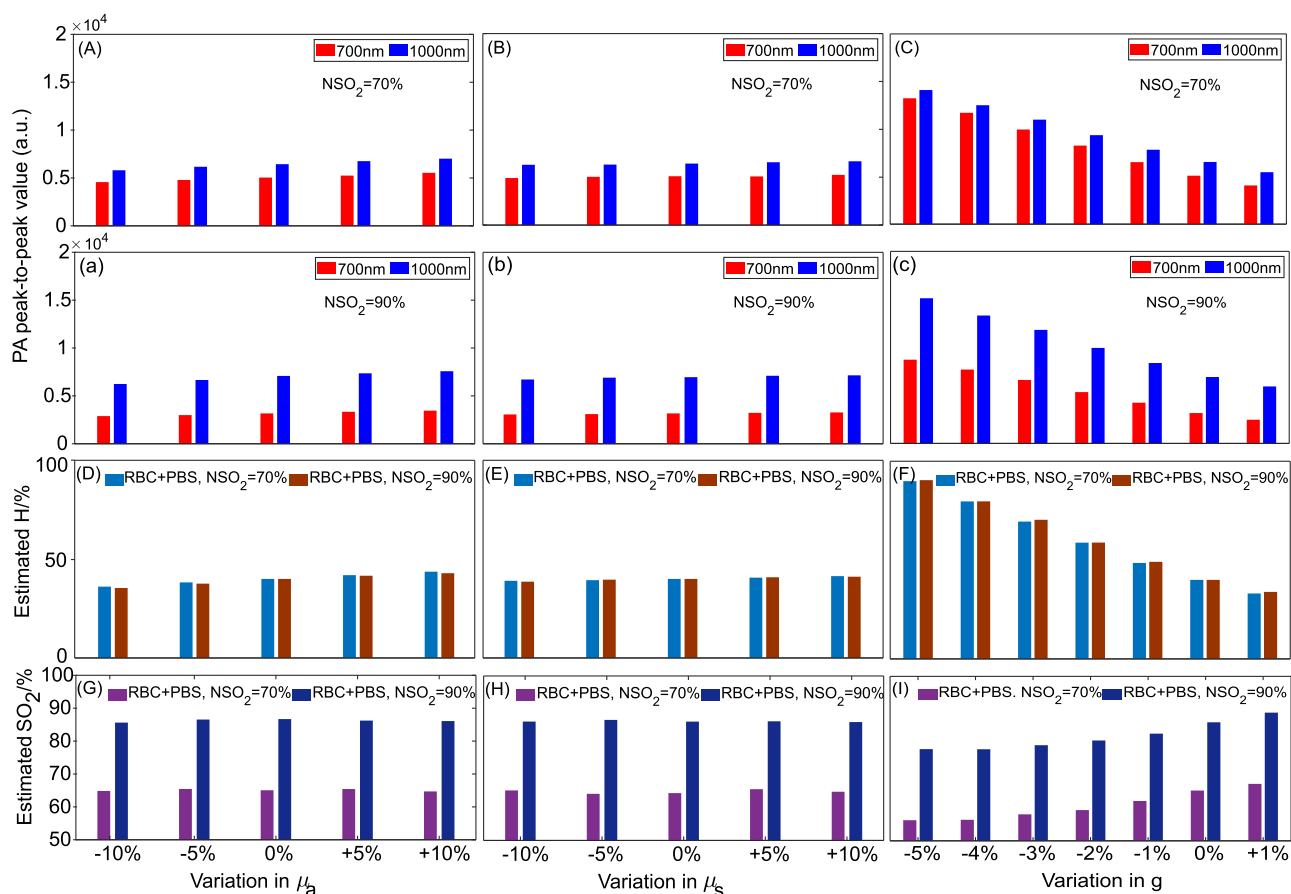
Fig. 7. Bar charts to show effects of variation of the optical parameters (μ_a, μ_s, and g) on the peak-to-peak amplitudes for 700 and 1000 nm wavelengths of the incident light (A)–(C), (a)–(c), respectively, hematocrit estimation (D)–(F), and SO_2 determination (G)–(I); μ_a and μ_s are varied from −10% to 10% with respect to the controls (i.e., 0%); g is changed from −5% to 1% compared to the control (i.e., 0%). For all samples, hematocrit is fixed to $H = 40\%$ (RBCs are suspended in PBS medium). Nominal SO_2 considered to be $NSO_2 = 70\%$ and 90%.

as the H level elevates with the deviation of g (see Figs. 8G–8I). This is also consistent with Fig. 6E.

4. DISCUSSION AND CONCLUSIONS

Hb/HbO molecules greatly absorb light energy at 532 nm making the absorption coefficient of blood very large at this wavelength. Therefore, optical penetration at 532 nm is the least but it is much higher at 700, 1000, and 1064 nm. It is very prominent at a physiological hematocrit (see rows 1–4, Fig. 4). It is also apparent from Fig. 4 that photons diffuse more into the RBC + PLS samples than the RBC + PBS prototypes (see columns 1, 2; 3, 4; 5, 6; and 7, 8). It is likely due to the fact that the g factor for an RBC + PLS sample is slightly higher than the corresponding RBC + PBS counterpart (see Figs. 2I–2L and rows 6, 9, 12, and 15 for $SO_2 = 70\%$; rows 21, 24, 27, and 30 for $SO_2 = 90\%$ of Supplement 1, Table S1). Theoretically, forward scattering vis-à-vis penetration depth increases as $g \to 1$. It may be mentioned here that the mismatch of refractive indices between RBC and PLS is less compared to that of RBC and PBS. As a result of that, light scatters more in the case of the latter sample.

The PA method has been extensively used to display tissue hemoglobin concentration and SO_2 maps in the context of

tomography and microscopy imaging. Hence, various combinations of optical wavelengths have been used to achieve the same [46,50,51]. This study also uses different incident laser beam pairs for probing the blood H and SO_2 levels. As expected, Fig. 5 confirms that H estimation does not depend on the choice of the wavelength pairs; however, for SO_2 estimation, accuracy is sensitive to the choice of the wavelengths of the incident light. In general, the SO_2 level can be faithfully estimated if the wavelengths of the incident light are situated on either side of the isosbestic point of blood absorption spectra (800 nm). Moreover, generally, 532 nm (one of the wavelengths) is not a good choice for assessing the blood SO_2 because light absorption is very strong in this wavelength and small fluctuations of the extinction coefficients for Hb and HbO (from the nominal values) may lead to a large error in the SO_2 estimation. The current study considers *in vitro* characterization of blood samples. However, the blood is usually embedded in a vessel within some sort of tissue whose constituents may have different light absorption properties. Therefore, the presence of other light absorbing components and complex geometries needs to be included in the model to examine how accurate the PA technique would be for quantifying the blood H and SO_2 under *in vivo* conditions.

This simulation study reveals that the absorbance map within a sample essentially depends upon the magnitude of
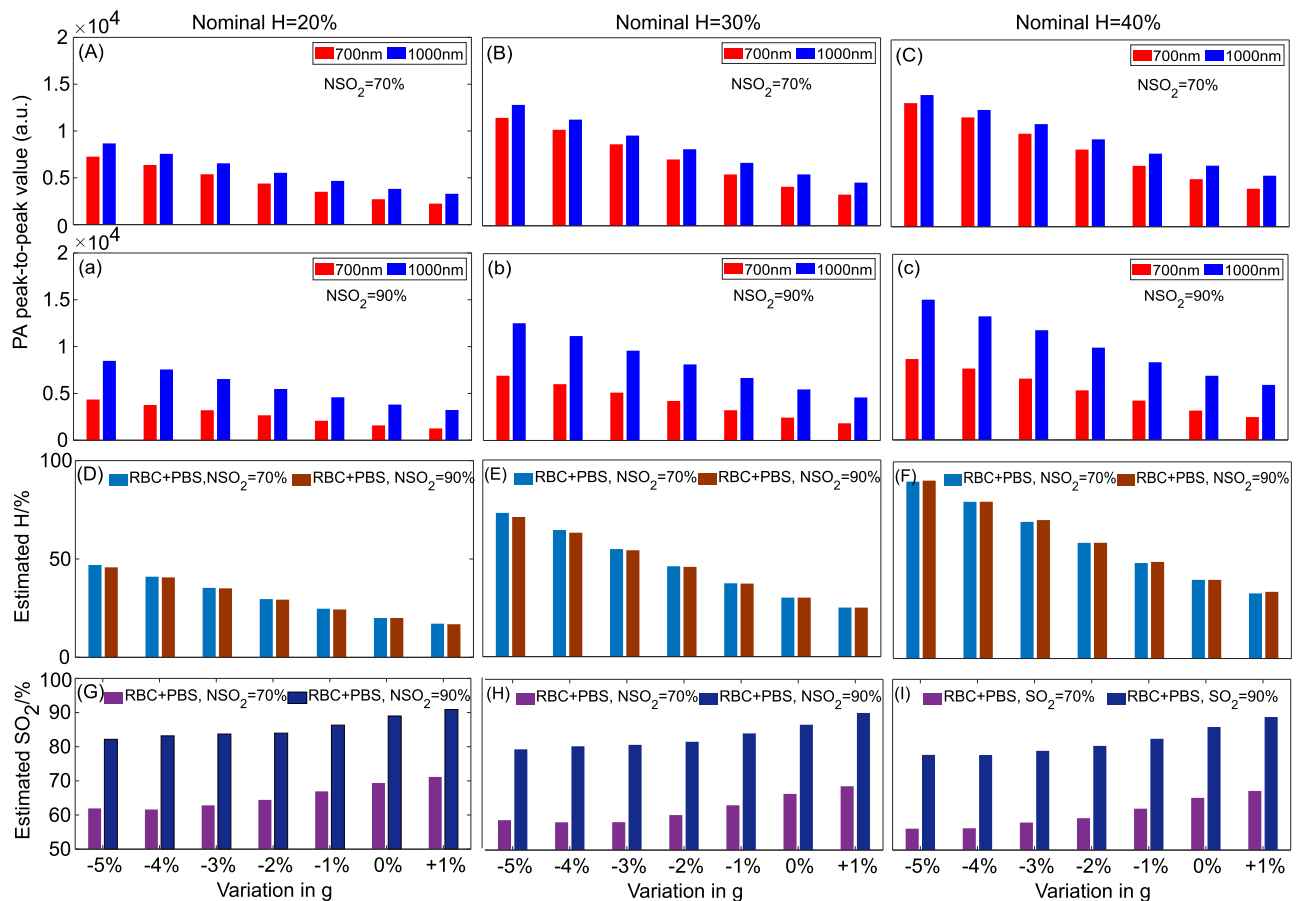
Fig. 8. Same as Fig. 7 but g parameter is changed and its impacts at various hematocrit levels are tested ($H = 20\%$, 30%, and 40%) for both the SO_2 levels.

its characteristic g parameter. The fluence map consequently dictates what would be the size and shape of the PA source. The absorbance maps for some representative cases are displayed in Supplement 1, Fig. S2. For example, the thickness of the PA source in the z-direction will increase but its width in the x-/y-direction will decrease when $g \approx 1$ (prefers forward scattering). As a result of that, PA pulse width will increase but pulse height will decrease. On the other hand, the thickness of the PA source in the z-direction will decrease but its width in the x-/y-direction will increase when $g < 1$ (promotes side scattering). In that case, the PA source will be converted into a thin but wide source. Hence, the PA pulse width will decrease but the amplitude of the PA pulse will greatly increase. A minute change in g value will alter the slope of a PA peak-to-peak amplitude versus nominal H graph. Thus, estimated SO_2 will significantly deviate from the nominal value. It may be mentioned here that the absorbance map also plays a crucial role in the context of near-infrared spectroscopy [52,53].

This simulation study reveals that the estimated H increases linearly when absorption coefficients are increased jointly (from -10% to 10% with respect to the nominal values); however, the accuracy of SO_2 estimation is independent of such changes. The assessment errors are indeed negligible even though the scattering coefficients are altered in the same range. Upon joint variation of the scattering anisotropy factor (at 700 and

1000 nm) by -5%, approximately 125% and 14% errors are introduced in the blood hematocrit and oxygen saturation estimations at $H = 40\%$, respectively. The scattering anisotropy factor has been found to be a very sensitive parameter and a small variation of this quantity can induce significant errors in the quantitative evaluations of blood characteristics. In the near future, we will conduct *in vitro* experiments with suspensions containing deformed/diseased RBCs and examine the performance of the PA technique in assessing blood H and SO_2 for pathological samples.

Disclosures. The authors declare no conflicts of interest regarding this paper.

Data availability. The dataset generated in this study is included in the paper.

Supplemental document. See Supplement 1 for supporting content.

REFERENCES

1. A. G. Bell, "On the production and reproduction of sound by light," in *Proceedings of the American Association for the Advancement of Science* (1881), Vol. **29**, pp. 115–136.

2. A. B. E. Attia, G. Balasundaram, M. Moothanchery, *et al.*, "A review of clinical photoacoustic imaging: current and future trends," Photoacoustics **16**, 100144 (2019).

3. S. Hu and L. V. Wang, "Photoacoustic imaging and characterization of the microvasculature," J. Biomed. Opt. **15**, 011101 (2010).

4. W. Choi, E.-Y. Park, S. Jeon, *et al.*, "Clinical photoacoustic imaging platforms," Biomed. Eng. Lett. **8**, 139–155 (2018).

5. C. Lee, M. Jeon, M. Y. Jeon, *et al.*, "*In vitro* photoacoustic measurement of hemoglobin oxygen saturation using a single pulsed broadband supercontinuum laser source," Appl. Opt. **53**, 3884–3889 (2014).

6. S. Jeon, J. Kim, D. Lee, *et al.*, "Review on practical photoacoustic microscopy," Photoacoustics **15**, 100141 (2019).

7. D.-K. Yao, K. Maslov, K. K. Shung, *et al.*, "*In vivo* label-free photoacoustic microscopy of cell nuclei by excitation of DNA and RNA," Opt. Lett. **35**, 4139–4141 (2010).

8. Y. Sun, E. Sobel, and H. Jiang, "Noninvasive imaging of hemoglobin concentration and oxygen saturation for detection of osteoarthritis in the finger joints using multispectral three-dimensional quantitative photoacoustic tomography," J. Opt. **15**, 055302 (2013).

9. S. Mondal, S. Paul, N. Singh, *et al.*, "Deep learning on photoacoustic tomography to remove image distortion due to inaccurate measurement of the scanning radius," Biomed. Opt. Express **14**, 5817–5832 (2023).

10. A. DiSpirito, III, T. Vu, M. Pramanik, *et al.*, "Sounding out the hidden data: a concise review of deep learning in photoacoustic imaging," Exp. Biol. Med. **246**, 1355–1367 (2021).

11. H. Shahid, A. Khalid, X. Liu, *et al.*, "A deep learning approach for the photoacoustic tomography recovery from undersampled measurements," Front. Neurosci. **15**, 598693 (2021).

12. M. Fribel, "Determination of optical properties of human blood in the spectral range 250 to 1100 nm using Monte Carlo simulations with hematocrit-dependent effective scattering phase functions," J. Biomed. Opt. **11**, 34021 (2006).

13. M. Meinke, G. Müller, J. Helfmann, *et al.*, "Optical properties of platelets and blood plasma and their influence on the optical behavior of whole blood in the visible to near infrared wavelength range," J. Biomed. Opt. **12**, 014024 (2007).

14. M. Friebel, J. Helfmann, U. Netz, *et al.*, "Influence of oxygen saturation on the optical scattering properties of human red blood cells in the spectral range 250 to 2000 nm," J. Biomed. Opt. **14**, 034001 (2009).

15. N. Bosschaart, G. J. Edelman, M. C. Aalders, *et al.*, "A literature review and novel theoretical approach on the optical properties of whole blood," Lasers Med. Sci. **29**, 453–479 (2014).

16. R. Hochuli, L. An, P. C. Beard, *et al.*, "Estimating blood oxygenation from photoacoustic images: can a simple linear spectroscopic inversion ever work?" J. Biomed. Opt. **24**, 121914 (2019).

17. C. Bench and B. Cox, "Quantitative photoacoustic estimates of intervascular blood oxygenation differences using linear unmixing," J. Phys. Conf. Ser. **1761**, 012001 (2021).

18. A. Sudakou, H. Wabnitz, A. Liemert, *et al.*, "Two-layered blood-lipid phantom and method to determine absorption and oxygenation employing changes in moments of DTOFs," Biomed. Opt. Express **14**, 3506–3531 (2023).

19. A. B. Karpiouk, S. R. Aglyamov, S. Mallidi, *et al.*, "Combined ultrasound and photoacoustic imaging to detect and stage deep vein thrombosis: phantom and ex vivo studies," J. Biomed. Opt. **13**, 054061 (2008).

20. E. Hysi, R. K. Saha, and M. C. Kolios, "Photoacoustic ultrasound spectroscopy for assessing red blood cell aggregation and oxygenation," J. Biomed. Opt. **17**, 125006 (2012).

21. R. K. Saha and M. C. Kolios, "Effects of erythrocyte oxygenation on optoacoustic signals," J. Biomed. Opt. **16**, 115003 (2011).

22. R. K. Saha, S. Karmakar, and M. Roy, "Photoacoustic response of suspended and hemolyzed red blood cells," Appl. Phys. Lett. **103**, 044101 (2013).

23. J. Brunker and P. Beard, "Erratum: Acoustic resolution photoacoustic doppler velocimetry in blood-mimicking fluids," Sci. Rep. **6**, 23881 (2016).

24. S. Banerjee, S. Sarkar, S. Saha, *et al.*, "Observing temporal variation in hemolysis through photoacoustics with a low cost laser diode based system," Sci. Rep. **13**, 7002 (2023).

25. F. J. Bodera, M. J. McVey, K. Sathiyamoorthy, *et al.*, "Detection of clot formation & lysis *in-vitro* using high frequency photoacoustic imaging & frequency analysis," Photoacoustics **30**, 100487 (2023).

26. P. P. Pai, P. K. Sanki, and S. Banerjee, "A photoacoustics based continuous non-invasive blood glucose monitoring system," in *IEEE International Symposium on Medical Measurements and Applications (MeMeA)* (IEEE, 2015), pp. 106–111.

27. R. M. Bateman, M. D. Sharpe, M. Singer, *et al.*, "The effect of sepsis on the erythrocyte," Int. J. Mol. Sci. **18**, 1932 (2017).

28. D. Balasubramanian, C. M. Rao, and B. Panijpan, "The malaria parasite monitored by photoacoustic spectroscopy," Science **223**, 828–830 (1984).

29. R. K. Saha, S. Karmakar, and M. Roy, "Computational investigation on the photoacoustics of malaria infected red blood cells," PLoS One **7**, e51774 (2012).

30. A. Kaushik and R. K. Saha, "Characterization of normal and deformed red blood cells using simulated differential photoacoustic cross-section spectral data," J. Phys. Commun. **5**, 035007 (2021).

31. R. K. Saha, "Predicting optoacoustic spectral behaviour of human erythrocytes, stomatocytes and echinocytes using a modified Green's function method," Eur. Biophys. J. **51**, 67–76 (2022).

32. F. Kibria, E. Hysi, E. M. Strohm, *et al.*, "Identification of red blood cell rouleaux formation using photoacoustic ultrasound spectroscopy," Proc. SPIE **8943**, 894367 (2014).

33. L. Wang, S. L. Jacques, and L. Zheng, "MCML—Monte Carlo modeling of light transport in multi-layered tissues," Comput. Methods Prog. Biomed. **47**, 131–146 (1995).

34. S. Wojtkiewicz and A. Liebert, "Parallel, multi-purpose Monte Carlo code for simulation of light propagation in segmented tissues," Biocybern. Biomed. Eng. **41**, 1303–1321 (2021).

35. A. Liemert and A. Kienle, "Light diffusion in N-layered turbid media: frequency and time domains," J. Biomed. Opt. **15**, 025002 (2010).

36. B. E. Treeby, B. T. Cox, and J. Jaros, "k-Wave: MATLAB toolbox for the simulation and reconstruction of photoacoustic wave fields," J. Biomed. Opt. **15**, 021314 (2010).

37. V. S. S. Konugolu, A. Farina, A. Dalla Mora, *et al.*, "Broadband (550–1350 nm) diffuse optical characterization of thyroid chromophores," Sci. Rep. **8**, 10015 (2018).

38. J. M. Steinke and A. Shepherd, "Comparison of Mie theory and the light scattering of red blood cells," Appl. Opt. **27**, 4027–4033 (1988).

39. J. K. Percus and G. J. Yevick, "Analysis of classical statistical mechanics by means of collective coordinates," Phys. Rev. **110**, 1–13 (1958).

40. V. Twersky, "Acoustic bulk parameters in distributions of pair-correlated scatterers," J. Acoust. Soc. Am. **64**, 1710–1719 (1978).

41. C. F. Bohren and D. R. Huffman, *Absorption and Scattering of Light by Small Particles* (Wiley, 2008).

42. S. Paul, H. S. Patel, V. Misra, *et al.*, "Numerical and in vitro experimental studies for assessing the blood hematocrit and oxygenation with the dual-wavelength photoacoustics," Photoaocustics, submitted for publication.

43. L. Yao, Y. Sun, and H. Jiang, "Quantitative photoacoustic tomography based on the radiative transfer equation," Opt. Lett. **34**, 1765–1767 (2009).

44. T. Saratoon, T. Tarvainen, B. Cox, *et al.*, "A gradient-based method for quantitative photoacoustic tomography using the radiative transfer equation," Inverse Prob. **29**, 075006 (2013).

45. S. L. Jacques, "Optical properties of biological tissues: a review," Phys. Med. Biol. **58**, R37–R61 (2013).

46. L. V. Wang and H.-I. Wu, *Biomedical Optics: Principles and Imaging* (Wiley, 2012).

47. B. T. Cox and P. C. Beard, "Fast calculation of pulsed photoacoustic fields in fluids using k-space methods," J. Acoust. Soc. Am. **117**, 3616–3627 (2005).

48. R. K. Saha and M. C. Kolios, "A simulation study on photoacoustic signals from red blood cells," J. Acoust. Soc. Am. **129**, 2935–2943 (2011).
49. A. Doronin and I. Meglinski, "Online object oriented Monte Carlo computational tool for the needs of biomedical optics," Biomed. Opt. Express **2**, 2461–2469 (2011).
50. P. Beard, "Biomedical photoacoustic imaging," Interface focus **1**, 602–631 (2011).
51. L. Meng, O. Deschaume, L. Larbanoix, *et al.*, "Photoacoustic temperature imaging based on multi-wavelength excitation," Photoacoustics **13**, 33–45 (2019).
52. H. Wabnitz, D. Contini, L. Spinelli, *et al.*, "Depth-selective data analysis for time-domain fNIRS: moments vs. time windows," Biomed. Opt. Express **11**, 4224–4243 (2020).
53. A. Sudakou, L. Yang, H. Wabnitz, *et al.*, "Performance of measurands in time-domain optical brain imaging: depth selectivity versus contrast-to-noise ratio," Biomed. Opt. Express **11**, 4348–4365 (2020).

Quantitative evaluation of the impact of variation of optical parameters on the estimation of blood hematocrit and oxygen saturation for dual-wavelength photoacoustics: supplement

SUBHADIP PAUL,[1] HARI SHANKAR PATEL,[2] AND RATAN K. SAHA[1,*] [ID]

[1]*Department of Applied Sciences, Indian Institute of Information Technology Allahabad, Prayagraj, 211015, India*
[2]*Laser Biomedical Applications Division, Raja Ramanna Centre for Advanced Technology, Indore, 452013, India*
*ratank.saha@iiita.ac.in

Quantitative evaluation of the impact of variation of optical parameters on the estimation of blood hematocrit and oxygen saturation for dual-wavelength photoacoustics: supplemental document

λ/nm	O. P.	SO$_2$ = 70%									
		H= 10%		H= 20%		H= 30%		H= 40%		H= 50%	
		PBS	PLS	PBS	PLS	PBS	PLS	PBS	PLS	PBS	PLS
532	μ_a/cm^{-1}	43.55	43.62	87.09	87.13	130.62	130.63	174.16	174.14	217.70	217.65
	μ_s/cm^{-1}	351.57	288.38	555.57	455.72	638.04	523.36	625.02	512.68	542.55	445.03
	g	0.976	0.979	0.976	0.979	0.976	0.979	0.976	0.979	0.976	0.979
700	μ_a/cm^{-1}	0.76	0.77	1.49	1.50	2.23	2.23	2.96	2.96	3.70	3.69
	μ_s/cm^{-1}	400.02	350.37	632.13	553.67	725.96	635.86	711.15	622.88	617.32	540.70
	g	0.988	0.993	0.988	0.993	0.988	0.993	0.988	0.993	0.988	0.993
1000	μ_a/cm^{-1}	1.31	1.21	2.18	2.12	3.04	3.03	3.91	3.94	4.77	4.84
	μ_s/cm^{-1}	309.22	256.68	488.65	405.62	561.19	465.83	549.74	456.32	477.20	396.11
	g	0.986	0.988	0.986	0.988	0.986	0.988	0.986	0.988	0.986	0.988
1064	μ_a/cm^{-1}	0.75	0.69	1.36	1.32	1.95	1.94	2.55	2.57	3.16	3.20
	μ_s/cm^{-1}	297.26	242.43	469.75	383.10	539.48	439.96	528.47	430.98	458.74	374.12
	g	0.986	0.988	0.986	0.988	0.986	0.988	0.986	0.988	0.986	0.988

λ/nm	O. P.	SO$_2$ = 90%									
		H= 10%		H= 20%		H= 30%		H= 40%		H= 50%	
		PBS	PLS	PBS	PLS	PBS	PLS	PBS	PLS	PBS	PLS
532	μ_a/cm^{-1}	45.36	45.42	90.70	90.73	136.04	136.05	181.38	181.36	226.72	226.67
	μ_s/cm^{-1}	351.57	288.38	555.57	455.72	638.04	523.36	625.02	512.68	542.55	445.03
	g	0.976	0.979	0.976	0.979	0.976	0.979	0.976	0.979	0.976	0.979
700	μ_a/cm^{-1}	0.47	0.48	0.92	0.92	1.37	1.37	1.82	1.81	2.27	2.25
	μ_s/cm^{-1}	400.02	350.37	632.13	553.67	725.96	635.86	711.15	622.88	617.32	540.70
	g	0.988	0.993	0.988	0.993	0.988	0.993	0.988	0.993	0.988	0.993
1000	μ_a/cm^{-1}	1.39	1.30	2.34	2.29	3.29	3.28	4.24	4.27	5.19	5.26
	μ_s/cm^{-1}	309.22	256.68	488.65	405.62	561.19	465.83	549.74	456.32	477.20	396.11
	g	0.986	0.988	0.986	0.988	0.986	0.988	0.986	0.988	0.986	0.988
1064	μ_a/cm^{-1}	0.81	0.74	1.46	1.42	2.12	2.11	2.77	2.79	3.42	3.47
	μ_s/cm^{-1}	297.26	242.43	469.75	383.10	539.48	439.96	528.47	430.98	458.74	374.12
	g	0.986	0.988	0.986	0.988	0.986	0.988	0.986	0.988	0.986	0.988

Table S1. The numerical values of the optical parameters (μ_a, μ_s and g) for different blood

samples for four different wavelengths of the incident light (532, 700, 1000 and 1064 nm). The oxygen saturation remained the same for all samples [SO_2 = 70% (top) and SO_2 = 90% (bottom)].

Variation/%	λ/nm	SO₂ = 70%	SO₂ = 90%	μs/cm⁻¹	g
		μₐ/cm⁻¹	μₐ/cm⁻¹		
-10	700	2.66	1.63	711.15	0.988
	1000	3.52	3.82	549.74	0.986
-5	700	2.81	1.72	711.15	0.988
	1000	3.71	4.03	549.74	0.986
0	700	2.96	1.82	711.15	0.988
	1000	3.91	4.24	549.74	0.986
+5	700	3.11	1.91	711.15	0.988
	1000	4.10	4.46	549.74	0.986
+10	700	3.26	2.00	711.15	0.988
	1000	4.30	4.67	549.74	0.986
-10	700	2.96	1.82	640.03	0.988
	1000	3.91	4.24	494.76	0.986
-5	700	2.96	1.82	675.59	0.988
	1000	3.91	4.24	522.25	0.986
0	700	2.96	1.82	711.15	0.988
	1000	3.91	4.24	549.74	0.986
+5	700	2.96	1.82	746.71	0.988
	1000	3.91	4.24	577.22	0.986
+10	700	2.96	1.82	782.26	0.988
	1000	3.91	4.24	604.71	0.986
-5	700	2.96	1.82	711.15	0.938
	1000	3.91	4.24	549.74	0.936
-4	700	2.96	1.82	711.15	0.948
	1000	3.91	4.24	549.74	0.946
-3	700	2.96	1.82	711.15	0.958
	1000	3.91	4.24	549.74	0.956
-2	700	2.96	1.82	711.15	0.968
	1000	3.91	4.24	549.74	0.966
-1	700	2.96	1.82	711.15	0.978
	1000	3.91	4.24	549.74	0.976
0	700	2.96	1.82	711.15	0.988
	1000	3.91	4.24	549.74	0.986
+1	700	2.96	1.82	711.15	0.997
	1000	3.91	4.24	549.74	0.995

Table S2. The computed values of the optical parameters (μ_a, μ_s and g) at 700 and 1000 nm wavelengths of the incident light for various test blood samples with fixed $H = 40\%$; two $SO_2 =$ 70% and 90% levels are considered; μ_a values at these wavelengths have been varied by $\pm 10\%$ with respect to the control (variation = 0%); μ_s values are altered by $\pm 10\%$ compared to the control (variation = 0%); g parameter in comparison to the control (variation = 0%) has been changed from -5% to 1% at each wavelength.

		$SO_2 = 70\%$								
Variation/%	λ/nm	H= 20%			H= 30%			H= 40%		
		μ_a/cm^{-1}	μ_s/cm^{-1}	g	μ_a/cm^{-1}	μ_s/cm^{-1}	g	μ_a/cm^{-1}	μ_s/cm^{-1}	g
-5	700	1.49	632.13	0.938	2.22	725.96	0.938	2.96	711.15	0.938
	1000	2.18	488.65	0.936	3.04	561.19	0.936	3.91	549.74	0.936
-4	700	1.49	632.13	0.948	2.22	725.96	0.948	2.96	711.15	0.948
	1000	2.18	488.65	0.946	3.04	561.19	0.946	3.91	549.74	0.946
-3	700	1.49	632.13	0.958	2.22	725.96	0.958	2.96	711.15	0.958
	1000	2.18	488.65	0.956	3.04	561.19	0.956	3.91	549.74	0.956
-2	700	1.49	632.13	0.968	2.22	725.96	0.968	2.96	711.15	0.968
	1000	2.18	488.65	0.966	3.04	561.19	0.966	3.91	549.74	0.966
-1	700	1.49	632.13	0.978	2.22	725.96	0.978	2.96	711.15	0.978
	1000	2.18	488.65	0.976	3.04	561.19	0.976	3.91	549.74	0.976
0	700	1.49	632.13	0.988	2.22	725.96	0.988	2.96	711.15	0.988
	1000	2.18	488.65	0.986	3.04	561.19	0.986	3.91	549.74	0.986
+1	700	1.49	632.13	0.997	2.22	725.96	0.997	2.96	711.15	0.997
	1000	2.18	488.65	0.995	3.04	561.19	0.995	3.91	549.74	0.995

		$SO_2 = 90\%$								
Variation/%	λ/nm	H= 20%			H= 30%			H= 40%		
		μ_a/cm^{-1}	μ_s/cm^{-1}	g	μ_a/cm^{-1}	μ_s/cm^{-1}	g	μ_a/cm^{-1}	μ_s/cm^{-1}	g
-5	700	0.92	632.13	0.938	1.37	725.96	0.938	1.82	711.15	0.938
	1000	2.34	488.65	0.936	3.29	561.19	0.936	4.24	549.74	0.936
-4	700	0.92	632.13	0.948	1.37	725.96	0.948	1.82	711.15	0.948
	1000	2.34	488.65	0.946	3.29	561.19	0.946	4.24	549.74	0.946
-3	700	0.92	632.13	0.958	1.37	725.96	0.958	1.82	711.15	0.958
	1000	2.34	488.65	0.956	3.29	561.19	0.956	4.24	549.74	0.956
-2	700	0.92	632.13	0.968	1.37	725.96	0.968	1.82	711.15	0.968
	1000	2.34	488.65	0.966	3.29	561.19	0.966	4.24	549.74	0.966
-1	700	0.92	632.13	0.978	1.37	725.96	0.978	1.82	711.15	0.978
	1000	2.34	488.65	0.976	3.29	561.19	0.976	4.24	549.74	0.976
0	700	0.92	632.13	0.988	1.37	725.96	0.988	1.82	711.15	0.988
	1000	2.34	488.65	0.986	3.29	561.19	0.986	4.24	549.74	0.986
+1	700	0.92	632.13	0.997	1.37	725.96	0.997	1.82	711.15	0.997
	1000	2.34	488.65	0.995	3.29	561.19	0.995	4.24	549.74	0.995

Table S3. Computed optical parameters for various blood samples with $H = 20\%$, 30%, 40% and $SO_2 = 70\%$, 90%. The scattering anisotropy (g) factor is evaluated at 700 and 1000 nm wavelengths. It is varied from -5% to +1%.
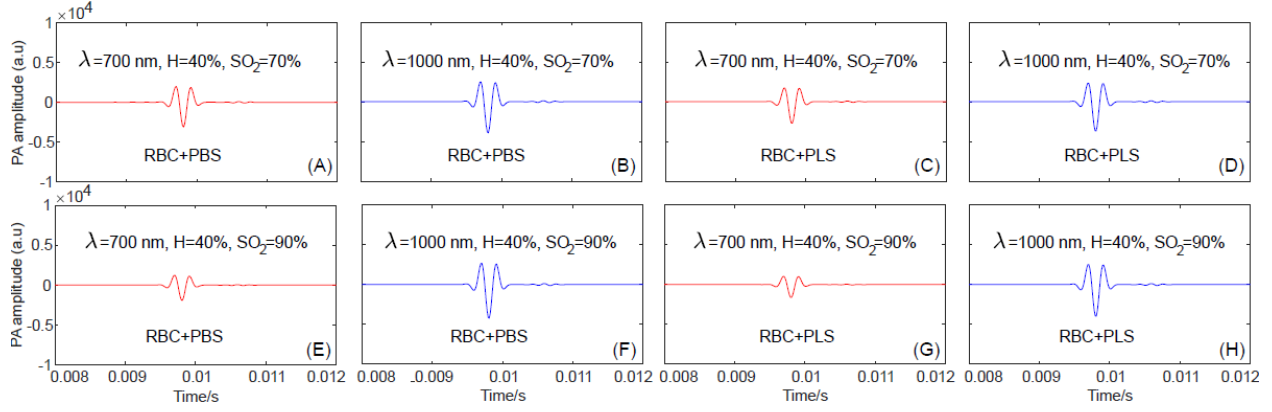
Fig. S1. Representative simulated PA signals at 700 nm and 1000 nm wavelengths, for RBC+PBS [(A), (B), (E), (F)] and RBC+PLS [(C), (D), (G), (H)] samples. The hematocrit and oxygen levels are provided in the legend of each figure.
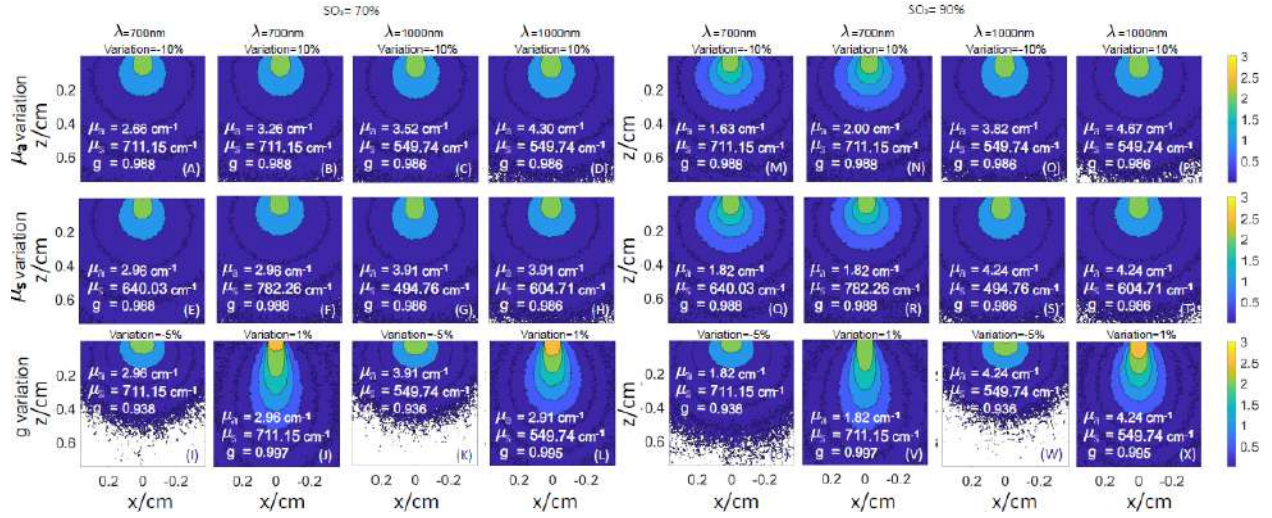
Fig. S2. The plots represent the generated spatial distribution of sensitivity to absorption at 700 nm and 1000 nm wavelengths, for variation in absorption coefficient μ_a [(A)-(D)], scattering coefficient μ_s [(E)-(H)] and g [(I)-(L)]; hematocrit level is fixed to $H = 40\%$.